RSC Advances

PAPER

View Article Online
View Journal | View Issue

Cite this: *RSC Adv.*, 2025, **15**, 301

Stabilization of small organic molecules on V_2C and V_2CO_2 MXenes: first-principles insights into the performance of van der Waals functionals and the effect of oxygen vacancies†

Thong Nguyen-Minh Le, *[ab] Thong Le Minh Pham, [cd] Thang Bach Phan [ef] and Yoshiyuki Kawazoe [ghi]

The adsorption of small organic molecules on pristine V_2C MXene and its derivatives is investigated by first-principles density functional theory calculations. By employing state-of-the-art van der Waals (vdW) density functionals, the binding affinity of studied molecules, *i.e.*, CH_4, CO_2, and H_2O on MXene adsorbents is well described by more recent vdW functionals, *i.e.*, SCAN-rvv10. Although both CH_4 and CO_2 are nonpolar molecules, on pristine and oxygen-vacancy surfaces, they show a different range of adsorption energies, in which CH_4 is more inert and has weaker binding than CO_2. CO_2 stays intact in its molecular forms for most of the tested functionals, except for the case of the vdW-DF functional, where CO_2 exhibits a dissociation regardless of its initial adsorption geometry. For full surface terminations, the adsorption affinity of all involved species is comparable within the same range, varying from −0.10 to −0.20 eV, attributed to either weak dispersion interactions or hydrogen bonds. The binding of H_2O is much more pronounced compared to CO_2 and CH_4 in the presence of oxygen vacancies with the highest adsorption energy of −1.33 eV, *vs.* −0.67, and −0.20 eV obtained for H_2O, CO_2, and CH_4 respectively. H_2O can dissociate with a small activation energy barrier of 0.40 eV, much smaller than its molecular adsorption energy, to further saturate itself on the surface. At high oxygen-vacancy concentrations, stronger bindings of adsorbates are found due to a preferred attachment of adsorbates to induced undercoordinated metal sites. The findings propose a potential scheme for greenhouse gas separation based on the surface modification of novel two-dimensional structures.

Received 15th September 2024
Accepted 18th December 2024

DOI: 10.1039/d4ra06676f

rsc.li/rsc-advances

1. Introduction

The interactions of organic molecules with metal surfaces are of great interest for both fundamental understanding and practical regulation, concerning many urgent adsorption and detection technology applications.[1–4] However, small organic molecules often encounter technical difficulties in adsorptive practices due to their inert properties. The binding of molecules onto the surface relies on both physical and chemical adsorption mechanisms.[5,6] Particularly, physisorption through van der Waals (vdW) interaction is known to be relevant for the attachment of nonpolar molecules,[7] in reverse to the binding of actively polar species relying on the exposure of chemical bonds. The treatment of such interactions is well-established for fist-principles calculations *via* the introduction of vdW functionals with either pairwise-additive vdW corrections,[8,9] or truly nonlocal vdW functionals.[10] Both approaches are successful in interpreting structures from biological molecules to layered compounds, as well as their physicochemical interactions.[11] Molecular binding affinities strongly depend on the activity of both the adsorbed molecules and the adsorbents, *i.e.*, the binding sites. Searching for suitable adsorbents for specific adsorbates is an indispensable prerequisite for advanced applications.

MXenes are novel layered materials emerging for relevant technologies based on their diverse structural compositions and stoichiometries, along with intriguing physical-chemical

[a]*Laboratory of Biophysics, Institute for Advanced Study in Technology, Ton Duc Thang University, Ho Chi Minh City, Vietnam. E-mail: lenguyenminhthong@tdtu.edu.vn*
[b]*Faculty of Pharmacy, Ton Duc Thang University, Ho Chi Minh City, Vietnam*
[c]*Institute of Research and Development, Duy Tan University, Da Nang 550000, Vietnam*
[d]*School of Engineering and Technology, Duy Tan University, Da Nang, 550000, Vietnam*
[e]*Center for Innovative Materials and Architectures, Ho Chi Minh City 700000, Vietnam*
[f]*Vietnam National University Ho Chi Minh City, Ho Chi Minh City 700000, Vietnam*
[g]*New Industry Creation Hatchery Center, Tohoku University, Sendai, 980-8579, Japan*
[h]*Department of Physics and Nanotechnology, SRM Institute of Science and Technology, Kattankulathur 603203, Tamil Nadu, India*
[i]*School of Physics, Institute of Science, Suranaree University of Technology, 111 University Avenue, Nakhon Ratchasima 30000, Thailand*

† Electronic supplementary information (ESI) available. See DOI: https://doi.org/10.1039/d4ra06676f

properties.[12] Those graphene-like structures can be experimentally synthesized *via* the exfoliation of "A" layer metals from its parent MAX phase $M_{n+1}AX_n$ by HCl or HF acids, followed by a sonification treatment to separate layers by layers.[13–15] The derived MXene surfaces are usually covered by terminal groups such as O, OH, or F in wet etching environments during the synthesis.[14,15] The chemical formula of a monolayer MXene is $M_{n+1}X_nT_x$, with X being the carbon C or nitrogen N sandwiched by early transition metals M (Sc, Ti, V, Mo, *etc.*, $n = 1, 2, 3$), and T_x (T = F, O, OH, $x = 0, 1, 2$) is the terminal groups. Those functional groups could be removed from the surface *via* chemical washing or thermal methods to obtain clean, pristine structures.[16,17] Featuring as high chemical and thermal stabilities, electrical conductivities, high surface areas, and abundant functional groups, MXenes are extensively studied for a variety of applications, especially for energy storage,[18–22] spintronics,[23] gas separation,[4] carbon capture,[24,25] gas sensors,[26–28] and catalysts.[29]

V_2C, a family member of carbon-based MXenes, has been known to be stable at 150 °C.[30] V_2CT_x, a functionalized form of V_2C, shows much superior by its high thermal stability, up to 300 °C in both oxidative and reductive environments, or up to 600 °C in inert environments.[16] Compared to the well-studied $Ti_3C_2T_x$ counterparts,[4,14,31] V_2CT_x benefits from its high surface area per mass and chemical activity relying on multiple oxidation states of V against Ti metal atoms.[32] V_2CT_x structures are widely studied as sensing materials to volatile organic compounds,[33,34] methane,[35] ammonia,[36] methylamine adsorption,[37] methylene blue removal,[38] carbon dioxide capture,[24,39] catalysts for hydrocarbon conversion,[40] or water dissociation.[41] Lee *et al.* experimentally reported an ultrahigh sensitivity of methane on V_2CT_x at room temperature provided that the functional groups are active sites for physical or chemical interactions.[35] A large number of M_2C (M = Ti, Zr, Hf, V, Nb, Ta, Cr, Mo, W) MXenes show strong bindings with carbon dioxide molecules compared to zeolites or graphene oxides.[39] Gouveia *et al.* computationally demonstrated that water can be dissociated on almost all pristine M_2X (M = Ti, Zr, Hf, V, Nb, Ta, Cr, Mo, and W) with low activation energy barriers.[41] Though many seminal works on the adsorption of organic molecules over V-based MXene structures can be found, bare MXene structures as adsorbents for small organic molecules are much more focused than the structures with the presence of explicit terminal groups or the existence of surface defects. The partial missing of terminating groups and the presence of other surface vacancies are inevitable in strongly acidic etching environments during the synthesis or in high thermal conditions for post-synthesis MXenes.[17,42,43] For example, terminal oxygens are most abundant, occupied about 84% terminations, among other functional groups on Ti_3C_2 MXene under synthesis conditions.[44] As a result, oxygen vacancies can be generated *via* multiple routes such as an incompletion termination during the synthesis, the chemical washing, or the thermal removal as post-synthesis modifications. Additionally, oxygen vacancies can also be produced and controlled by the oxidation of carbon monoxide on the MXene surface, under the presence of H_2, *via* the chemical reaction, $CO + H_2 + MXene \rightarrow HCOOH + MXene\_O_v$, proposed by Zhang and coworkers.[45] In this work, the oxygen vacancy on Ti_2CO_2 plays the role of a catalytic site for capturing and driving CO_2 reduction. To enhance the catalytic activity, single transition-metal atoms are deposited to the oxygen-vacant sites featuring the efficiency of oxygen evolution reactions[46] on Mo_2CO_2 and the methane-to-methanol conversion on $V_3C_2O_2$.[47] It has been known that bare MXenes without terminations are very active in capturing most of the molecules by chemical bonds relying on top-layer transition metals.[25,41] Besides, functionalized MXenes, as V_2CT_x, characterize rich surface chemistry exhibiting hydrophilic features due to their O- or OH-terminated groups, favoring hydrogen bondings or weak vdW interactions.[48,49] The presence of surface defects on functionalized structures proposes more active sites at realistic conditions. The hybrid of multiple phases by surface engineering is advantageous for the efficient treatment of mixed gases.

Systematic insights into the response of V_2CT_x MXenes against small organic molecules, *i.e.*, greenhouse gases, regarding their adsorption mechanisms and affinities are fundamentally and technologically important. This work provides the interaction trends of both polar and nonpolar molecules with the V_2CT_x MXenes focusing on their adsorption performances on either the pristine, functionalized, or defective surfaces. Based on first-principles calculations, we attempt to benchmark the stability of adsorbed molecules at their binding sites concerning the choice of van der Waals functionals. The more advanced vdW functionals will be used for further calculations. The functionalizations and defect modifications allow us to better determine the selectivity of various target molecules. Following the adsorption, the calculated dissociation processes are the key signals showing the activity of the induced surface sites, in which the oxygen vacancies play a paramount importance role.

2. Computational method

Calculations based on density functional theory (DFT) are performed on the simulation suite Vien *Ab initio* Simulation Package (VASP 5.4.4).[50] The project augmented wave (PAW) pseudopotential[51] with a cutoff kinetic energy of 500 eV is chosen for all atoms. The lattice parameters of the host structures and adsorption affinities of gas molecules are evaluated under the light of generalized gradient approximation (GGA) functionals of Perdew, Burke, and Ernzerhof (PBE),[52,53] and PBE with a D3 correction scheme.[8] The nonlocal van der Waals functionals of optPBE-vdW,[54] optB88-vdW,[54] vdW-DF,[55] and rev-vdW-DF2 (ref. 56) are also included to improve long-range interactions of adsorbates. In addition, the *meta*-GGA functional of SCAN-rvv10 (ref. 57) is also used to benchmark either the intralayer lattice constants or the long-range binding of molecular adsorptions. For optimizations, the atoms are allowed to relax until the atomic force exerted on each atom balances at 0.01 eV $Å^{-1}$ and the convergence of the total energy of 10^{-5} eV.

Spin-polarization is applied for all calculated structures to account for the magnetic feature of the vanadium atoms. We

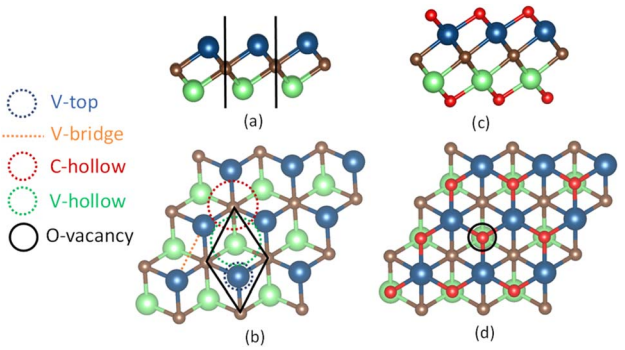

Fig. 1 Monolayers of 3 × 3 sizes are displayed in the side-view and top-view for the pure V_2C, in (a) and (b), and functionalized V_2CO_2, in (c) and (d), respectively. The spheres in blue, green, brown, and red correspond to vanadium V on the top layer, V on the bottom layer, carbon C, and oxygen O atoms. The adsorption sites on the surface are denoted as V-top, V-bridge, C-hollow, V-hollow, and O-vacancy (O_v). The C-hollow and V-hollow sites are located in the center of three V atoms with the underneath C and V atoms, respectively. The black lines in (a) and rhombus in (b) define the boundaries of the primitive cell in the side and top view, respectively.

first benchmark the primitive cells 1 × 1 of V_2C and V_2CO_2 using 9 × 9 × 1 *k*-point meshes within the Gamma sampling scheme. For the adsorption study, structures of 3 × 3 are directly generated from the previous pre-optimized primitive cells, shown in Fig. 1. For all calculations, a vacuum slab of at least 17 Å is chosen, which is sufficiently large to ignore spurious interactions. The oxygen-vacancy V_2CO_2_O_v configuration is also produced by removing one functionalized-oxygen atom. The *k*-point meshes of 3 × 3 × 1 are now used for all the adsorption calculations. The electron configurations of involving atoms are as follows V: [Ar] $4s^2$ $3d^3$, C: [He] $2s^2$ $2p^2$, O: [He] $2s^2$ $2p^4$, and H: $1s^1$. The isolated gas molecules CH_4, H_2, CO_2, and H_2O are modeled in a cubic box of 20 Å length in each dimension. The adsorption energy E_{ads} of a molecule M is defined as eqn (1),

$$E_{ads} = E_{M\text{-host}} - E_M - E_{host} \quad (1)$$

where $E_{M\text{-host}}$, E_M, and E_{host} stand for the total energies of the structures of the host with the adsorbed molecule, isolated molecule, and pristine structure, respectively. Excluding a surface oxygen atom costs an amount of energy as follows eqn (2),

$$E_{O_v} = E_{host\text{-}O_v} + \frac{1}{2}E_{O_2} - E_{host} \quad (2)$$

where $E_{host\text{-}O_v}$, E_{O_2}, and E_{host} are the total energies of the oxygen-vacancy structure, isolated molecular oxygen, and pristine structure, respectively. The Mulliken charge analysis employed in LOBSTER code[58] (Local Orbital Basis Suite Towards Electronic-Structure Reconstruction) is used to evaluate atomic charges of the structures before and after adsorptions. The VESTA visualizing program, version 3.5.7,[59] is exploited to display all geometries. The transition state search is performed under the climbing-image nudged elastic band (CINEB) method.[60] Accordingly, nine intermediate images along the reaction path are generated and optimized. The obtained transition state is further confirmed by the fact that there is only one imaginary frequency corresponding to the transition mode of the interested reaction channel.

3. Result and discussion

3.1 Geometry optimization

Monolayer pristine V_2C is obtained by manually eliminating atomic aluminum layer "Al" from the MAX phase V_2AlC unit cell, a layered hexagonal cell of the $P6_3/mmc$ space group (space group number 194).[31,61] The V_2C primitive cell, shown in Fig. 1(a) and (b), is composed of three atoms arranged in ternary atomic layers, where carbon atoms are sandwiched between top and bottom vanadium atoms. The primitive cell is optimized in the way that lattice constants "*a*" and "*b*" are simultaneously increased or decreased, followed by the relaxation of atomic positions, until its optimal total energy is found. The lattice constants for the primitive cells of both pristine V_2C and V_2CO_2 are calculated within various functionals, including references to the previous work,[62] as the results are shown in Table 1. For V_2C, it was found that the first four used functionals, *i.e.*, PBE, PBE-D3, optPBE-vdW, and optB88-vdW, have similar lattice constants of about 2.89–2.90 Å and V–V distances of 2.16–2.17 Å, while vdW-DF predicts those values as high as 2.92 Å and 2.21 Å, respectively. Conversely, the functionals rev-vdW-DF2 and SCAN-rvv10 provide smaller values of only 2.87–2.88 Å and 2.18–2.19 for the lattice constants and V–V distances, respectively.

Table 1 Optimized parameters with different exchange–correlation functionals for the primitive cell, a tetragonal geometry. Lattice constants "*a*" and "*b*" are equal. The expansion of intra-atomic layers is determined by the distance between the top and bottom V atoms d_{V-V}. The bond length d_{V-O} is defined as the average distance of the V atom to the three connected surface oxygen atoms

Lattice constant (Å)		vdW functional							
		PBE	PBE-D3	optPBE-vdW	optB88-vdW	vdW-DF	Rev-vdW-DF2	SCAN-rvv10	Ref. 62
V_2C	$a = b$	2.90	2.89	2.90	2.90	2.92	2.88	2.87	2.89[a]
	d_{V-V}	2.16	2.17	2.16	2.16	2.21	2.19	2.18	2.18[a]
V_2CO_2	$a = b$	2.90	2.89	2.90	2.90	2.94	2.89	2.87	2.90[a]
	d_{V-V}	2.38	2.37	2.42	2.41	2.45	2.38	2.39	2.38[a]
	d_{V-O}	1.95	1.95	1.96	1.96	1.98	1.95	1.94	N/A

[a] Calculated with a PBE method.[62]

For V_2CO_2, we have seen that "*a*" and "*b*" are almost unchanged or slightly increased for all functionals. The expansion of the intra-atomic layers in the "*c*" direction, or the functionalized orientation, is obvious by the increase of V–V distances of around 0.19–0.26 Å (~10%) compared to ones for V_2C for all the functionals, see Table 1, V_2CO_2, d_{V-V}. Among benchmarked functionals, vdW-DF shows its highest lattice parameters and atomic-layer distances, while SCAN-rvv10 is on the reverse. This also implies that bond lengths described by vdW-DF are more elongated and debilitated than others. Accordingly, as shown in Table 1, the average V–O bond lengths, d_{V-O}, for vdW-DF is the longest, about 1.98 Å compared to other functionals. SCAN-rvv10 predicts this bond length is only 1.94 Å, which is the shortest one.

Obtaining the most compact V_2CT_X structures by SCAN-rvv10 is important to distinguish their energetic performances related to structural modifications.

3.2 Adsorption of CH_4, CO_2 and H_2O

Terminated by V^{1+} atoms, V_2C adsorbate is very active in the binding of small gas molecules through different adsorption mechanisms. Functionalizing of V_2C with –O groups causes a reduction of V^{1+} to V^{2+} due to the strong negativity of surface oxygen atoms. The surface chemistry of V_2CO_2 is subsequently dominated by the presence of terminated groups O^{1-}. Fig. 2 shows all the adsorption geometries of small molecules over both V_2C and V_2CO_2. The atomic positions for each structure are provided in the ESI, Section S1.†

3.2.1 Adsorption affinity

3.2.1.1 CH_4. CH_4, a nonpolar molecule, is inactive for binding to many materials. CH_4 molecules can be captured by metal atoms *via* an electrostatic interaction.[63–65] Here, CH_4 molecules prefer binding to V-top atoms on the V_2C surface with a η^2 mode, see Fig. 2(a). This adsorption geometry agrees well with previous works, where CH_4 resides on top of single metal atoms.[64–66] The electrostatic attraction arises from the surface V^{1+} atom and a partially negative charge of carbon C of the CH_4 molecule. The adsorption energies vary from a weak binding of less than 0.10 eV to a few eV depending on the performance of functionals, as shown in Table 2, entry 1, and Fig. 3(a). It can be seen that there is a large discrepancy in values derived from different functionals. Similar adsorption energies could be found in groups of PBE, PBE-D3, and SCAN-rvv10 functionals, while the other functionals show overbinding of CH_4 being larger than unity. On V_2CO_2, CH_4 molecules attach to the C-hollow site with three hydrogen atoms pointing towards surface oxygens, so-called a η^3-like mode, see Fig. 2(d). There is another configuration, *i.e.*, a η^2-like mode, in which the energy is only about 2 meV smaller than the η^3-like one accounted for SCAN-rvv10. The adsorption energies are higher for most of the functionals upon the functionalization compared to ones on the pristine, except for rev-vdW-DF2 and SCAN-rvv10. Considering equilibrium distances between CH_4 and the V_2CO_2 surface, it has been found that SCAN-rvv10 estimated a shortest distance of 2.90 Å, compared to the values of greater than 3.0 Å for the others. Expectedly, SCAN-rvv10 provides the upper limit with a small binding energy of 0.11 eV for CH_4 against various vdW-corrected functionals, *cf.* Table 2, entry 2. For the presence of O_v, the overall trend is inverse, as shown in Fig. 3(a), adsorption energies are enhanced for rev-vdW-DF2 and SCAN-rvv10 (see Table 2, entry 3), while it shows decreasing for other functionals.

3.2.1.2 CO_2. On the pristine V_2C, CO_2 molecules form very strong chemical bonds with surface V atoms with high adsorption energies of −2.0 eV to over −4.0 eV for all the investigated functionals. Here, the π orbitals of CO_2 and d-orbitals of metals are hybridized in a way of the so-called Dewar mechanism,[67] resulting in such pronounced binding affinity. The most stable adsorption is found, in which CO_2 is

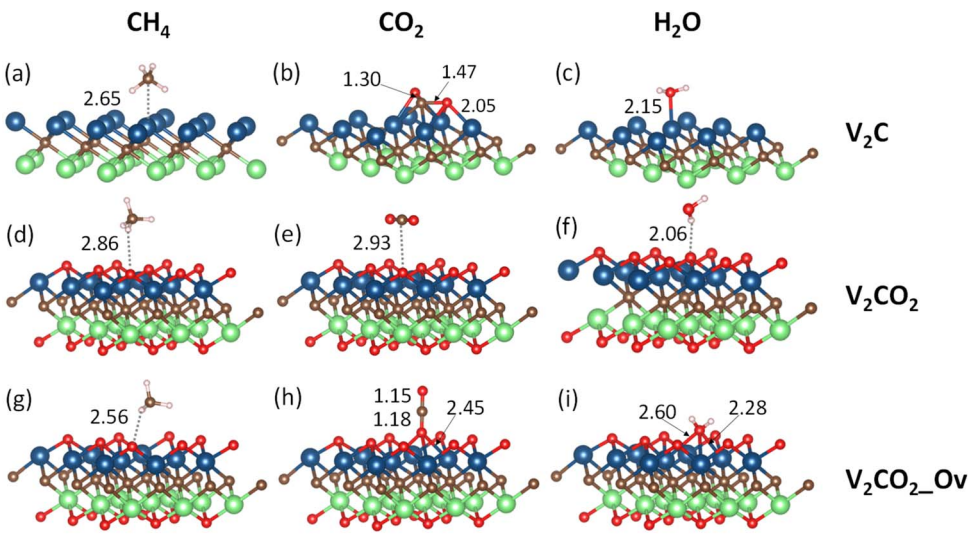

Fig. 2 Most stable adsorption configurations are shown for all investigated molecules. The labels (a and b), and (c–e), and (f–i) denote the adsorption of target molecules on V_2C, V_2CO_2, and V_2CO_2_O_v, respectively. The displayed numbers (in Å), calculated *via* SCAN-rvv10, show either the bond lengths or nearest distances (dash lines) between the molecules and surface atoms.

Table 2 Adsorption energies (in eV) for the most stable adsorption configurations. The adsorbed species retain their molecular states on the V_2CT_x surface unless otherwise noted. On the pristine V_2C surface, CH_4 binds to the V atom *via* a η^2 mode, H_2 resides on the V-top site with a side-on geometry, CO_2 prefers bridging configuration, while H_2O prefers V-top configuration. Three entries in each molecule correspond to the adsorption of that molecule on the pristine V_2C, V_2CO_2, and V_2CO_2_O_v, respectively

		vdW functional						
Gas/V_2CT_x		PBE	PBE-D3	optPBE-vdW	optB88-vdW	vdW-DF	rev-vdW-DF2	SCAN-rvv10
CH_4	1	−0.01	−0.35	−1.99	−1.94	−2.63	−1.26	−0.25
	2	−0.35	−0.36	−2.46	−2.29	−3.24	−1.19	−0.11
	3	−0.02	−0.33	−2.11	−1.98	−2.73	−1.32	−0.20
CO_2	4	−2.00	−3.52	−3.41	−3.62	−4.43[a]	−2.55	−2.60
	5	−0.22	−0.41	−0.68	−0.61	−0.79	−0.17	−0.18
	6	−0.09	−0.49	−0.49	−0.53	−0.79	−0.53	−0.67
H_2O	7	−0.72	−0.95	−0.84	−0.85	−0.68	−0.88	−0.97
	8	−0.40	−0.38	−0.61	−0.53	−0.73	−0.35	−0.16
	9	−0.79	−1.17	−1.06	−1.10	−0.92	−1.20	−1.33

[a] Dissociated into CO and O fragments.

strongly bent from its linear structure, as shown in Fig. 2(b). C and two O atoms prefer residing on the V-hollow and C-hollow sites, respectively. This geometry corresponds to the most stable adsorption model, *i.e.*, η^3-CO_2-μ^5-$C_MO_CO_C$, found by Á. Morales-García and co-workers in the earlier work.[39] Particularly, we have seen that CO_2 easily breaks into –CO and –O fragments on the pristine V_2C surface calculated with vdW-DF functional regardless of initial adsorption configurations, while CO_2 can keep its molecular structure for other functionals. The adsorption energy for CO_2 is −4.43 eV for vdW-DF, much higher than

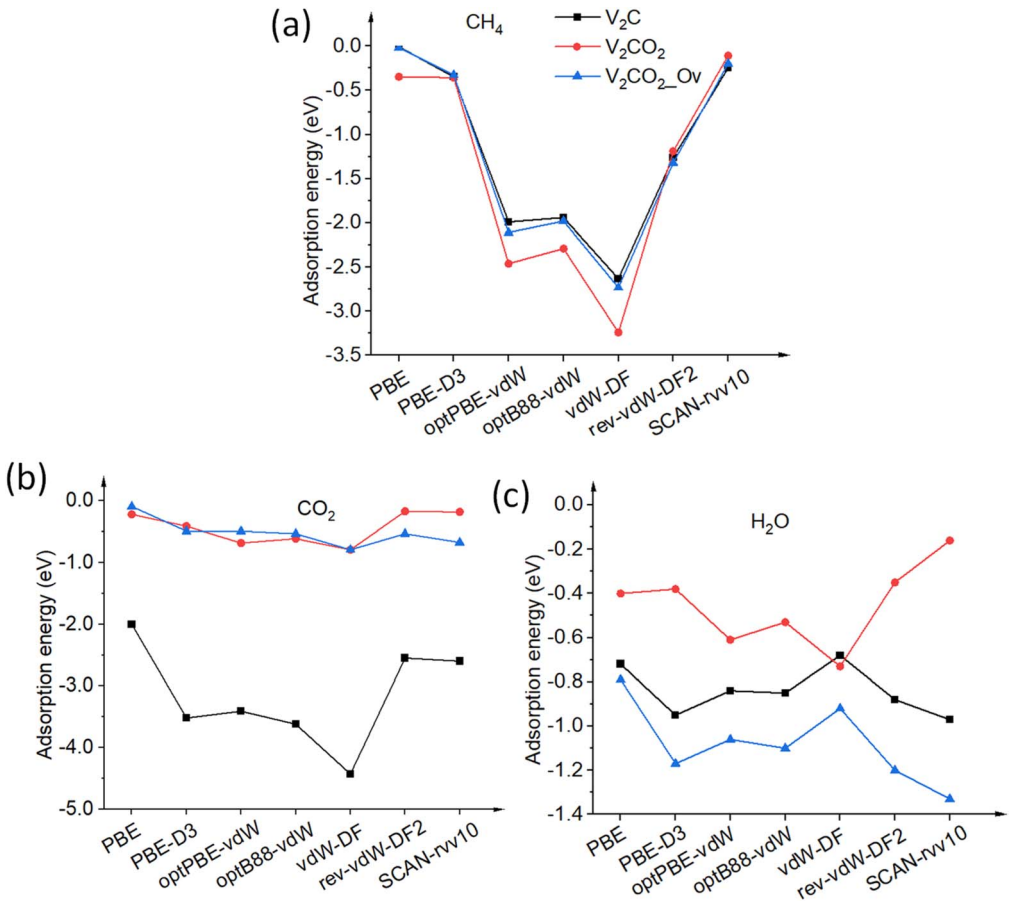

Fig. 3 Adsorption energies E_{ads} of molecules (a) CH_4, (b) CO_2, and (c) H_2O on pristine V_2C and its functionalized structures are calculated with various van der Waals functionals. The solid lines connected points to points are for eye guidance.

others due to the breaking of the O–CO bond, see value in Table 2, entry 4. On V_2CO_2 adsorbate, vdW binding is much smaller than chemical one for all functionals, see Fig. 2. On V_2CO_2_O_v, CO_2 molecules occupy the O_v sites with a single-bond geometry, see Fig. 2(h). This preferable orientation of nonpolar CO_2 significantly enhances its adsorption energies concerning PBE-D3, rev-vdW-DF2, and SCAN-rvv10, from −0.41, −0.17, and −0.18 eV to −0.49, −0.53, and −0.67 eV, respectively. Those functionals are appropriate for the treatment of such chemical bonds.

3.2.1.3 H_2O. H_2O molecules are most stable and stay intact at V-top sites, see Fig. 2(c), among possible adsorption sites on the V_2C surface. Calculated with SCAN-rvv10, the binding energy for H_2O located at the V-bridge is about 5 meV lower than the V-top one. All functionals well predict adsorption energies without much difference, in a range of −0.68 to −0.97 eV, *cf.* Table 2, entry 7. PBE-D3 and SCAN-rvv10 provide very similar values of −0.95 and −0.97 eV, respectively. On V_2CO_2, it is dominated by the hydrogen bonding between terminating group O and H of H_2O, see Fig. 2(f). The adsorption energy shifts towards lower binding of H_2O compared to the pristine one, as shown in Fig. 3(c). The functional vdW-DF exhibits an exception by showing overbinding of H_2O *via* hydrogen bond against the chemical bond, *i.e.*, −0.73 *vs.* −0.68 eV, respectively, while SCAN-rvv10 pronouncedly softens this binding with only −0.16 eV. In the presence of an oxygen-vacant O_v site, all the functionals show their high adsorption affinity towards the occupation of H_2O compared to those on the pristine. Here, H_2O is bound to top-layer vanadium atoms *via* a triple-bond geometry, see Fig. 2(i), based on three dangling bonds remaining due to the missing functional groups –O. In this case, the energy trend derived for all functionals is identical to the one for V_2C concerning the chemical bonding mechanism. SCAN-rvv10 shows its highest adsorption energy among other functionals with −1.33 eV, while vdW-DF is still underestimated with only −0.92 eV, see Table 2, entry 9.

3.2.2 Insight into the electronic property. To determine the effect of adsorption on the electronic structure of host structures, the density of states (DOS) is plotted, as shown in Fig. 4–6, for V_2C, V_2CO_2, and V_2CO_2_O_v, respectively. Compared to the gas phase, the DOS of bonding states are shifted to lower energy regions. The shift is larger for stronger bindings and *vice versa*. For CH_4 adsorption, the pristine V_2C surface noticeably modifies σ_p rather than σ_s, as can be seen in Fig. 4(a). Accordingly, σ_p is broader in the adsorbed state compared to the one near the Fermi level in the gas phase. This electronic structure modification is because of a transferring of 0.16*e* from the surface to CH_4, as presented in Table 3. For CH_4 adsorbed on V_2CO_2 and V_2CO_2_O_v, weak binding of CH_4 is exhibited by a relative shifting of peaks without the influence of the hosts, as plotted in Fig. 5(a) and 6(a), respectively. For CO_2, high charge transferring from the V_2C, about 1.34*e*, see Table 3, causes a broadening of the $1\pi_u$ peak in the adsorbed state, at around −7.5 eV, along with a strong reduction of DOS of the host V_2C

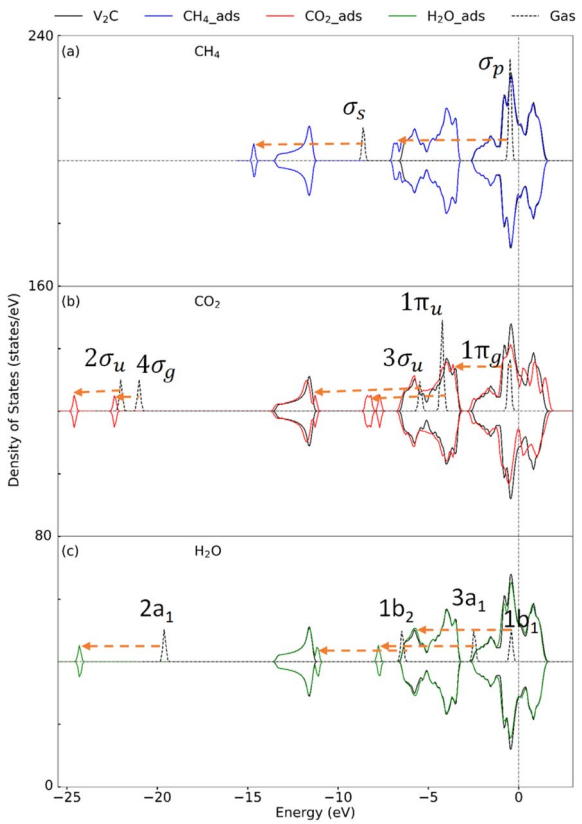

Fig. 4 Density of state for the adsorption of (a) CH_4, (b) CO_2, and (c) H_2O on V_2C. Dashes arrows indicate shifting of the peaks.

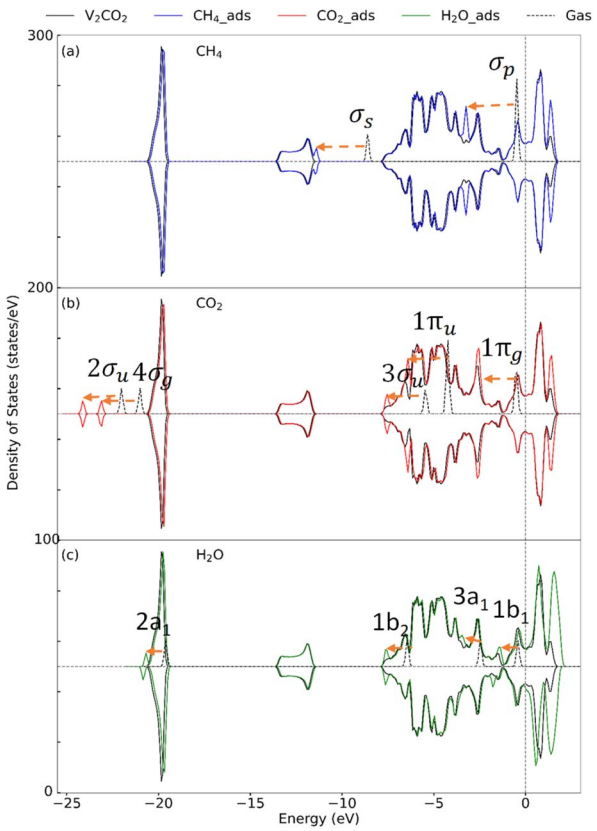

Fig. 5 Density of state for the adsorption of (a) CH_4, (b) CO_2, and (c) H_2O on V_2CO_2. Dashes arrows indicate shifting of the peaks.

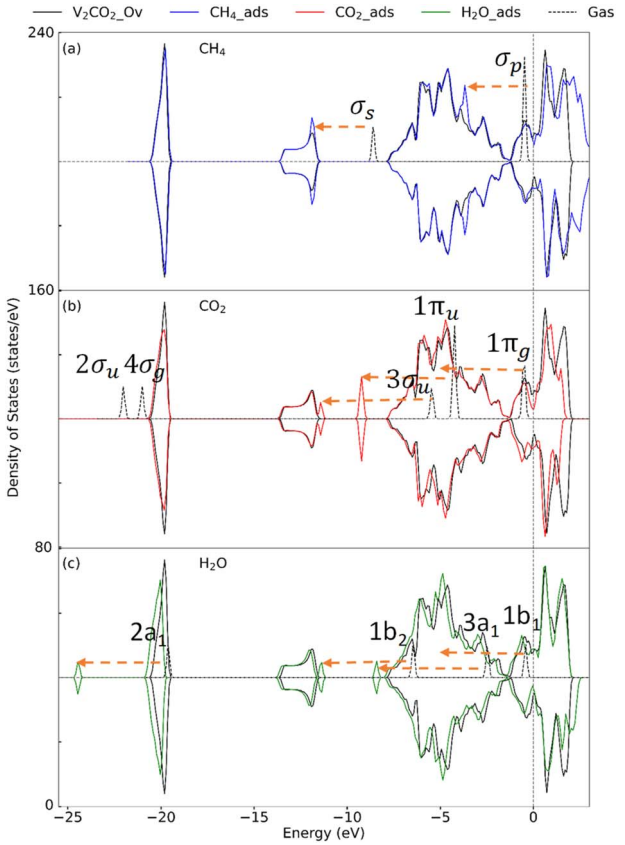

Fig. 6 Density of state for the adsorption of (a) CH_4, (b) CO_2, and (c) H_2O on V_2CO_2_O_v. Dashes arrows indicate shifting of the peaks.

Table 3 The charge transfer between the V_2CT_X surfaces and adsorbed molecules. The positive and negative values indicate the charge donating from the surface to the adsorbate and vice *versus*, respectively

	Charge transfer (e)		
V_2CT_X	CH_4	CO_2	H_2O
V_2C	0.16	1.34	−0.03
V_2CO_2	0.02	0.01	0.00
V_2CO_2_O_v	0.09	−0.06	−0.09

near the Fermi level, as plotted in Fig. 4(b). There is also a strong fluctuation of DOS near the Fermi level due to the preferable binding of CO_2 at the vacant site on V_2CO_2_O_v, see Fig. 6(b), compared to the unchanged state on V_2CO_2, shown in Fig. 5(b). For H_2O adsorption, we see that the DOS of the systems are almost similar on V_2C and V_2CO_2 before and after adsorption, while there is a clear lowering shift of the DOS on V_2CO_2_O_v in response to a saturation of adsorbed H_2O at the vacant site.

3.3 Oxygen-vacancy effects

3.3.1 Vacancy formation energy. We first determine whether chemical bond strengths depend on the choice of functionals or not by considering the energy cost, or formation energy of vacancy, of eliminating one functional oxygen atom. The calculated result is shown in Fig. 7. All the obtained formation energies are over 2 eV, indicating chemical bonds are formed between surface oxygen and the underlying vanadium atoms. It can be seen that PBE and vdW-DF provide similar formation energies of around 2.65 eV, well in agreement with the literature,[17] of which are smaller than other tested functionals. Formation energy values for PBE-D3, optPBE, and optB88 together distribute over a higher range from 2.90 to 3.10 eV, while ones for rev-vdW-DF2 and SCAN-rvv10 are most pronounced at about 3.20–3.30 eV. Higher formation energies obtained by rev-vdW-DF2 and SCAN-rvv10 are consistent with the fact that V–O bond lengths of these structures are nearest, as mentioned in Section 3.1, leading to stronger binding of O atoms. The trend of formation energy found here also reflects an overestimation of lattice constants and atomic distances of vdW-DF functional, where the bond lengths and bond strengths between atoms are longer and weaker. The bond lengths are improved by other functionals in the tested group, particularly for SCAN-rvv10, and so for the binding of terminal oxygen atoms.

3.3.2 High vacancy regime. The second and third oxygen atoms are further removed from the surface to generate double- and triple-oxygen vacancies. Here, only the nearest neighbors are considered resulting in two- and three-body cluster defects. The calculated formation energies of single-, double-, and triple-oxygen vacancies obtained by SCAN-rvv10 are 3.28, 3.59, and 4.05 eV, respectively. This implies the formation energies tend to increase for higher defect concentrations. Regarding the adsorption, Table 4 shows the influence of vacancy concentration, *i.e.*, 1/9, 2/9, and 3/9 ML, on the adsorption affinity. As higher oxygen vacancy densities, the adsorption energies of all adsorbates significantly increase, about −0.20 to −0.40 eV, at the highest concentration of 3/9 ML, in response to binding

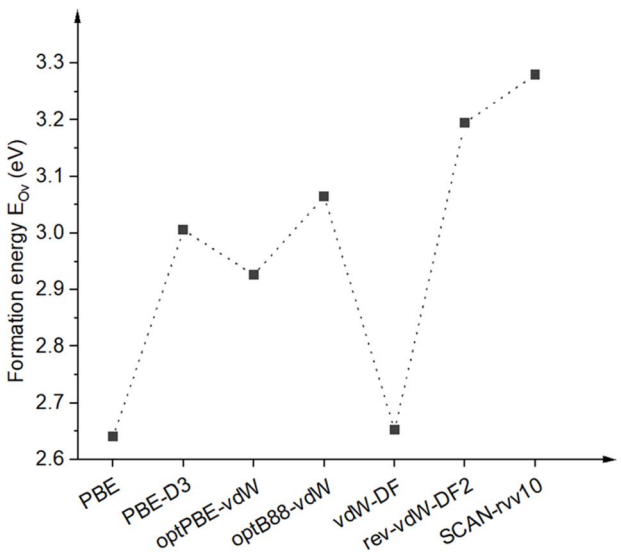

Fig. 7 Formation energies of oxygen vacancy E_{O_v} were calculated for different van der Waals functionals. The dashed line is for eye guidance.

Table 4 Adsorption energy (eV) at high vacancy concentrations. The single, double, and triple oxygen vacancies are denoted as 1/9 ML, 2/9 ML, and 3/9 ML, respectively. ML stands for "monolayer". 9 is the total number of identical adsorption sites on the investigation surface

	Oxygen-vacancy concentration		
Gas	1/9 ML	2/9 ML	3/9 ML
CH_4	−0.20	−0.22	−0.64
CO_2	−0.67	−0.52	−0.87
H_2O	−1.33	−1.27	−1.58

preference to undercoordinated vanadium atoms induced by removing the functional groups. Accordingly, for 3/9 ML, CH_4 molecules retain their η^2 binding modes, similar to the one on the pristine V_2C, while CO_2 and H_2O molecules attach atop under-coordinated surface vanadiums through monodentate configurations. Those adsorption geometries are provided in the ESI, Section S2.† For 2/9 ML, a slight decrease in the binding of CO_2 and H_2O is found, which might be the competition between the structural change and the adsorption.

3.3.3 Adsorption and dissociation of adsorbed H_2O molecules. It has been introduced in the previous section that the absence of surface atomic oxygen creates dangling bonds as active sites for the capturing of target molecules. Among investigated species, H_2O, followed by CO_2, show their highest affinities towards the O_v sites to saturate undercoordinated vanadium atoms. Calculated by SCAN-rvv10 functional, there is a significant energy shift from −0.16 eV to −1.33 eV *via* the hydrogen-to-chemical bond concerning before and after the presence of O_v, respectively. This adsorption could be characterized by considering the vibrational modes of H_2O before and after binding. Accordingly, we have obtained a lowering of about 200 cm^{-1} for asymmetry and symmetry stretching modes of adsorbed H_2O compared to its isolated gas-phase counterpart, *i.e.*, 3698 and 3606 *vs.* 3963 and 3848 cm^{-1}, respectively, while the bending modes are unaffected. This happens in response to the small elongation of O–H bond lengths from 0.96 to 0.97 Å for adapting from the isolated-to-adsorbed states. Moreover, upon binding to undercoordinated vanadium atoms, adsorbed H_2O reveals a weak charge withdrawal of about 0.09 *e* from surface V atoms for its stabilization. Through first-principles molecular dynamics simulations, the early work on $Ti_3C_2O_2$, a family of V_2CT_x, showed that H_2O can recover the oxygen at the oxygen-vacancy site by its decomposition reaction, however, it did not address the dissociative barrier.[68] In this work for V_2CO_2, Fig. 8 shows the calculated energy path along the dissociation channel for H_2O with the intrinsic energy barrier. Adsorbed at O_v site, or IS, one of the hydrogen atoms of H_2O leaves its bonding state and hops to the available neighboring oxygen site, depicted as transition state (TS) and final state (FS) geometries in Fig. 8. For the TS, the activation barrier for this dissociation is small at 0.40 eV, approximately corresponding to the temperature activation of 140 K by heating or electron exposure,[69] calculated by SCAN-rvv10 functional, while it is found to be 0.30 eV by PBE-D3 as a reference. The imaginary frequency is approximately 1400 cm^{-1} in magnitude for SCAN-rvv10, compared to 1126 cm^{-1} obtained by PBE-D3, corresponding to a stretching vibration of the hydrogen atom. This relatively low energy is attributed to a pre-elongation of the H–O bond of adsorbed H_2O and the presence of the nearby functionalized active center –O for the stabilizing of the dissociated-unbound hydrogen atom.

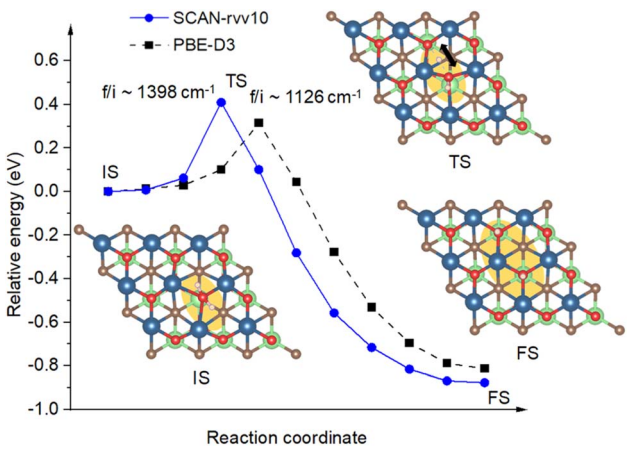

Fig. 8 The energy paths, calculated with SCAN-rvv10, with a reference *via* PBE-D3, are shown for the dissociation of H_2O initiated at O_v sites. It also includes the geometries of adsorption/initial state (IS), transition state (TS), and final state (TS). The orange background highlights the active region of H_2O on the surface for a top view. The imaginary frequencies denoted as "*f*/i" are provided for transition states. The black arrow indicates the vibrational direction of the dissociated hydrogen atom at the TS.

Fig. 9 displays the density of state (DOS) for the structures before and after functionalization, the structure with an oxygen vacancy, and the adsorbed H_2O. Compared between Fig. 9(a) and (b), it can be seen that the oxygen functionalization results in the shift of the entire bonding region around the Fermi level, down to −5.0 eV, because more bondings are formed between V and surface oxygen at the O_v site. The DOS of V atoms becomes broadened for both bonding and antibonding states upon missing surface oxygen at that site, see Fig. 9(c). This is beneficial for the adsorption of water molecules, which its DOS is plotted in Fig. 9(d). The O_p orbital of the O atom in H_2O replaces the role of O_v, however, it shows a weaker binding to V than O_v with fewer bonding states around the Fermi level. We can see here that three more peaks, *i.e.*, p1, p2, and s, appear concerning the hybridizations of O_s and O_p orbitals of H_2O with the s orbital of H. One of the O_p peaks, *i.e.* p1, is higher in energy, and closer to the Fermi level, than the others. At the TS state, Fig. 9(e), the peak p1 is broadened and smaller, showing the weakening of the O–H bond in water. For the final state, the DOS is shown in Fig. 9(f), a new p3 state appears in between p1 and p2 in energy corresponding to the formation of the surface O–H bonding states. The closer orbital energy of the p1 peak against the Fermi level, or in other words closer to DOS of nearby oxygens, enhances the dissociation of water with a small barrier aforementioned and further stabilizes surface oxygens. This is important in showing the potential vacancy-adsorption site for actively catalytic occurrences.

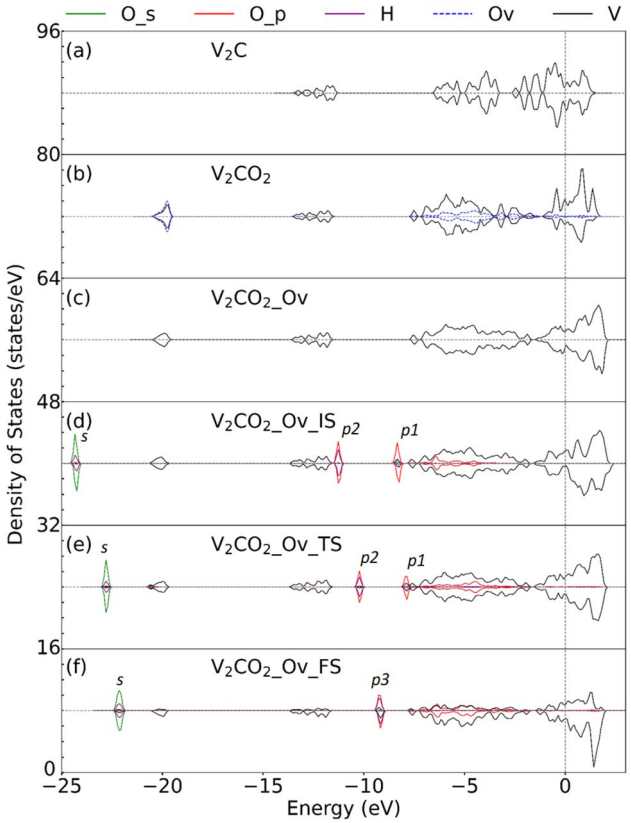

Fig. 9 The projected density of state (PDOS) represents the change in molecular states upon the adsorption and dissociation of H_2O molecules. The subfigure (a)–(c) are the PDOS for the pristine V_2C, O-functionalized V_2CO_2, and oxygen vacancy V_2CO_2–O_v, respectively. The PDOS of H_2O at the O_v site is plotted in (d)–(f) for the adsorption, transition, and final states, respectively. O_s, O_p, and H correspond to the s and p orbitals of O, and the hydrogen atom in H_2O. O_v represents the functionalized oxygen atom at the vacancy site. Here, we only consider the DOS of three V atoms connected to O_v, presented by the black line. The vertical dash line at 0 eV indicates the Fermi level.

4. Conclusions

We study the stability and energetic performances of small organic molecules over V_2C and V_2CT_x by employing first-principles DFT-based calculations. It was demonstrated that commonly used pairwise-additive and nonlocal vdW functionals can similarly describe the adsorption affinity of both polar and nonpolar molecules on V_2CT_x. Recently developed van der Waals functionals, *i.e.*, rev-vdW-DF2 or SCAN-rvv10, are more rational for energetic performances by lessening or enhancing the binding of nonpolar and polar molecules such as CH_4 and H_2O, respectively. The early vdW functional, *i.e.*, vdW-DF, obviously overestimates the atomic bond lengths of both host and target molecules resulting in the adsorption dissociations of extremely stable CO_2 molecules on the pristine surface. For full terminations, adsorption energies, *i.e.*, less than −0.20 eV, are on the same scale for the studied gases showing the binding strengths of weak vdW or hydrogen bonding types. High selectivity is observed for oxygen-vacancy structures with the preferred binding of H_2O at the vacant sites *via* the chemical bonds. Upon the adsorption, the charges are found to be transferred from the surface to the adsorbed molecules for the pristine V_2C and in an opposite direction for the oxygen vacancy surfaces. The adsorption causes shifting of the DOS toward a lower energy range, resulting in more stable configurations and strong changes in the density of states near the Fermi levels. Higher oxygen-vacancy concentrations offer stronger bindings of all adsorbates relying on the coordination at the vacancy-induced vanadium sites. Preadsorbed single water molecule proceeds a dissociation channel with a small activation barrier, about 0.40 eV, in response to the close orbital overlaps of adsorbed and functionalized atoms. The oxygen-vacancy site serves as an active center for both capturing and activating such dissociation reactions. The different energetics for specific structural phases of adsorptions suggest that CH_4, CO_2, and H_2O respond similarly in full termination surfaces. However, a small number of single-atom defects presented, *i.e.*, oxygen vacancies, enhance the adsorption of H_2O, followed by CO_2. Further removing functional groups, resulting in a pristine surface, is beneficial for the capture of CO_2 only. Our work provides a potential scheme for greenhouse gas separation applications provided that control of the surface chemistry is pivotal in realistic conditions. Certainly, the positions and concentrations of vacancies should be considered and manipulated completely on purpose. In such circumstances, experimental validation is highly valuable not only for greenhouse gas treatment as in this study but also for activating other adsorbates. The engineering of functionalized MXene surfaces paves the way for the enhancement of its chemical activities regarding its multiple roles as binding sites, catalysts, or catalyst beds. Consequently, it is essential to establish an intrinsic correlation between vacancy density and catalytic activity. The co-adsorption of target molecules is also another issue in practice. For example, the clustering of water molecules might happen to the hydrophilic MXene surfaces, influencing either the adsorptive affinity or catalytic activity, which has been disregarded in the current work. All these factors are greatly attributed to both fundamental understandings and practical performances that should be carefully taken into account.

Data availability

The data supporting this article have been included as part of the ESI.†

Conflicts of interest

There are no conflicts to declare.

Acknowledgements

The authors greatly acknowledge the Center for Innovative Materials and Architectures, Vietnam National University Ho Chi Minh City, Vietnam, Institute for Materials Research, Tohoku University, Japan, and the Institute of Atomic and Molecular Sciences, Academia Sinica, Taiwan for providing authorized computational packages, as well as high-

performance computing resources. T. N. M. L. would like to thank Dr Jer-Lai Kuo at the Institute of Atomic and Molecular Sciences, Academia Sinica, Taiwan for the assistance.

References

1 W. Liu, A. Tkatchenko and M. Scheffler, *Acc. Chem. Res.*, 2014, **47**, 3369–3377.
2 W. Liu, F. Maass, M. Willenbockel, C. Bronner, M. Schulze, S. Soubatch, F. S. Tautz, P. Tegeder and A. Tkatchenko, *Phys. Rev. Lett.*, 2015, **115**, 036104.
3 S. Mehdi Aghaei, A. Aasi and B. Panchapakesan, *ACS Omega*, 2021, **6**, 2450–2461.
4 S. Massoumilari and S. Velioglu, *ACS Omega*, 2023, **8**, 29859–29909.
5 A. Tkatchenko, L. Romaner, O. T. Hofmann, E. Zojer, C. Ambrosch-Draxl and M. Scheffler, *MRS Bull.*, 2011, **35**, 435–442.
6 J. E. Lennard-Jones, *Trans. Faraday Soc.*, 1932, **28**, 333–359.
7 K. Berland, C. A. Arter, V. R. Cooper, K. Lee, B. I. Lundqvist, E. Schroder, T. Thonhauser and P. Hyldgaard, *J. Chem. Phys.*, 2014, **140**, 18A539.
8 S. Grimme, S. Ehrlich and L. Goerigk, *J. Comput. Chem.*, 2011, **32**, 1456–1465.
9 N. Marom, A. Tkatchenko, M. Rossi, V. V. Gobre, O. Hod, M. Scheffler and L. Kronik, *J. Chem. Theory Comput.*, 2011, **7**, 3944–3951.
10 D. Chakraborty, K. Berland and T. Thonhauser, *J. Chem. Theory Comput.*, 2020, **16**, 5893–5911.
11 K. Berland, V. R. Cooper, K. Lee, E. Schroder, T. Thonhauser, P. Hyldgaard and B. I. Lundqvist, *Rep. Prog. Phys.*, 2015, **78**, 066501.
12 Y. Gogotsi and B. Anasori, *ACS Nano*, 2019, **13**, 8491–8494.
13 M. Naguib, V. N. Mochalin, M. W. Barsoum and Y. Gogotsi, *Adv. Mater.*, 2014, **26**, 992–1005.
14 A. Iqbal, J. Hong, T. Y. Ko and C. M. Koo, *Nano Convergence*, 2021, **8**, 9.
15 V. Shukla, *Mater. Adv.*, 2020, **1**, 3104–3121.
16 R. Thakur, A. VahidMohammadi, J. Moncada, W. R. Adams, M. Chi, B. Tatarchuk, M. Beidaghi and C. A. Carrero, *Nanoscale*, 2019, **11**, 10716–10726.
17 J. D. Gouveia and J. R. B. Gomes, *Phys. Rev. Mater.*, 2022, **6**, 024004.
18 Z. Xu, X. Lv, J. Chen, L. Jiang, Y. Lai and J. Li, *Phys. Chem. Chem. Phys.*, 2017, **19**, 7807–7819.
19 L. Wang, D. Liu, W. Lian, Q. Hu, X. Liu and A. Zhou, *J. Mater. Res. Technol.*, 2020, **9**, 984–993.
20 K. Han, Y. Ji, Q. Hu, Q. Wu, D. Li and A. Zhou, *Phys. Chem. Chem. Phys.*, 2024, **26**, 18030–18040.
21 Q. Wu, Z. Wang, Q. Hu, Y. Ji, D. Li, J. Wang, Q. Xia, L. Wang and A. Zhou, *Phys. Chem. Chem. Phys.*, 2023, **25**, 14406–14416.
22 Q. Hu, Y. Ji, D. Li, Z. Wang, K. Han, Q. Wu, J. Wang, Q. Xia, L. Wang and A. Zhou, *Phys. Chem. Chem. Phys.*, 2023, **25**, 9428–9436.
23 S. Li, Y. Wang, Y. Wang, S. Sanvito and S. Hou, *J. Phys. Chem. C*, 2021, **125**, 6945–6953.
24 I. Persson, J. Halim, H. Lind, T. W. Hansen, J. B. Wagner, L. A. Naslund, V. Darakchieva, J. Palisaitis, J. Rosen and P. O. A. Persson, *Adv. Mater.*, 2019, **31**, e1805472.
25 R. Morales-Salvador, J. D. Gouveia, Á. Morales-García, F. Viñes, J. R. B. Gomes and F. Illas, *ACS Catal.*, 2021, **11**, 11248–11255.
26 D. H. Ho, Y. Y. Choi, S. B. Jo, J. M. Myoung and J. H. Cho, *Adv. Mater.*, 2021, **33**, e2005846.
27 J. T. Mazumder and R. K. Jha, *Sens. Actuators Rep.*, 2023, **6**, 100174.
28 Q. Hu, W. Liu, D. Li, Q. Wu, Y. Chang, J. Wang, Q. Xia, L. Wang and A. Zhou, *Mater. Today Commun.*, 2024, **40**, 109467.
29 M. Keyhanian, D. Farmanzadeh, Á. Morales-García and F. Illas, *J. Mater. Chem. A*, 2022, **10**, 8846–8855.
30 M. Wu, B. Wang, Q. Hu, L. Wang and A. Zhou, *Mater.*, 2018, **11**, 2112.
31 M. Naguib, M. Kurtoglu, V. Presser, J. Lu, J. Niu, M. Heon, L. Hultman, Y. Gogotsi and M. W. Barsoum, *Adv. Mater.*, 2011, **23**, 4248–4253.
32 K. Matthews, T. Zhang, C. E. Shuck, A. VahidMohammadi and Y. Gogotsi, *Chem. Mater.*, 2021, **34**, 499–509.
33 M. Wu, Y. An, R. Yang, Z. Tao, Q. Xia, Q. Hu, M. Li, K. Chen, Z. Zhang, Q. Huang, S.-h. Ma and A. Zhou, *ACS Appl. Nano Mater.*, 2021, **4**, 6257–6268.
34 S. M. Majhi, A. Ali, Y. E. Greish, H. F. El-Maghraby and S. T. Mahmoud, *Sci. Rep.*, 2023, **13**, 3114.
35 E. Lee, A. VahidMohammadi, Y. S. Yoon, M. Beidaghi and D. J. Kim, *ACS Sens.*, 2019, **4**, 1603–1611.
36 N. Liu, J. Li, S. Ma and Z. Jiao, *Phys. E*, 2023, 148.
37 N. Salami, *Appl. Surf. Sci.*, 2022, **581**, 152105.
38 H. Lei, Z. Hao, K. Chen, Y. Chen, J. Zhang, Z. Hu, Y. Song, P. Rao and Q. Huang, *J. Phys. Chem. Lett.*, 2020, **11**, 4253–4260.
39 Á. Morales-García, A. Fernández-Fernández, F. Viñes and F. Illas, *J. Mater. Chem. A*, 2018, **6**, 3381–3385.
40 R. Thakur, M. Hoffman, A. VahidMohammadi, J. Smith, M. Chi, B. Tatarchuk, M. Beidaghi and C. A. Carrero, *ChemCatChem*, 2020, **12**, 3639–3643.
41 J. D. Gouveia, Á. Morales-García, F. Viñes, F. Illas and J. R. B. Gomes, *Appl. Catal., B*, 2020, **260**, 118191.
42 A. Bandyopadhyay, D. Ghosh and S. K. Pati, *Phys. Chem. Chem. Phys.*, 2018, **20**, 4012–4019.
43 R. Ibragimova, P. Rinke and H.-P. Komsa, *Chem. Mater.*, 2022, **34**, 2896–2906.
44 M. A. Hope, A. C. Forse, K. J. Griffith, M. R. Lukatskaya, M. Ghidiu, Y. Gogotsi and C. P. Grey, *Phys. Chem. Chem. Phys.*, 2016, **18**, 5099–5102.
45 X. Zhang, Z. Zhang, J. Li, X. Zhao, D. Wu and Z. Zhou, *J. Mater. Chem. A*, 2017, **5**, 12899–12903.
46 S. Ram, G. H. Choi, A. S. Lee, S.-C. Lee and S. Bhattacharjee, *J. Phys. Chem. C*, 2023, **127**, 12576–12585.
47 J. Xu, T. Wang, C. Geng, Y. Zhen, M. Lin, Z. Huang, Y. Shi, L. Zhao and W. Xing, *ACS Appl. Nano Mater.*, 2024, **7**, 20974–20984.
48 S. Jung, U. Zafar, L. S. K. Achary and C. M. Koo, *EcoMat*, 2023, **5**, e12395.

49 A. Junkaew and R. Arroyave, *Phys. Chem. Chem. Phys.*, 2018, **20**, 6073–6082.
50 G. Kresse and J. Hafner, *Phys. Rev. B:Condens. Matter Mater. Phys.*, 1993, **47**, 558–561.
51 P. E. Blochl, *Phys. Rev. B:Condens. Matter Mater. Phys.*, 1994, **50**, 17953–17979.
52 J. P. Perdew, K. Burke and M. Ernzerhof, *Phys. Rev. Lett.*, 1996, **77**, 3865–3868.
53 J. P. Perdew, K. Burke and M. Ernzerhof, *Phys. Rev. Lett.*, 1997, **78**, 1396.
54 J. Klimes, D. R. Bowler and A. Michaelides, *J. Phys.:Condens. Matter*, 2010, **22**, 022201.
55 M. Dion, H. Rydberg, E. Schroder, D. C. Langreth and B. I. Lundqvist, *Phys. Rev. Lett.*, 2004, **92**, 246401.
56 I. Hamada, *Phys. Rev. B:Condens. Matter Mater. Phys.*, 2014, **89**, 121103(R).
57 H. Peng, Z.-H. Yang, J. P. Perdew and J. Sun, *Phys. Rev. X*, 2016, **6**, 041005.
58 S. Maintz, V. L. Deringer, A. L. Tchougreeff and R. Dronskowski, *J. Comput. Chem.*, 2016, **37**, 1030–1035.
59 K. Momma and F. Izumi, *J. Appl. Crystallogr.*, 2011, **44**, 1272–1276.
60 G. Henkelman, B. P. Uberuaga and H. Jónsson, *J. Chem. Phys.*, 2000, **113**, 9901–9904.
61 M. Naguib, O. Mashtalir, J. Carle, V. Presser, J. Lu, L. Hultman, Y. Gogotsi and M. W. Barsoum, *ACS Nano*, 2012, **6**, 1322–1331.
62 A. Champagne, L. Shi, T. Ouisse, B. Hackens and J.-C. Charlier, *Phys. Rev. B*, 2018, **97**, 115439.
63 G. W. Roffe and H. Cox, *J. Phys. Chem. A*, 2013, **117**, 3017–3024.
64 O. V. Lushchikova, S. Reijmer, P. B. Armentrout and J. M. Bakker, *J. Am. Soc. Mass Spectrom.*, 2022, **33**, 1393–1400.
65 T. N.-M. Le, T. B. N. Le, P. T. Nguyen, T. T. Nguyen, Q. N. Tran, T. T. Nguyen, Y. Kawazoe, T. B. Phan and D. M. Nguyen, *RSC Adv.*, 2023, **13**, 15926–15933.
66 S. Impeng, P. Khongpracha, J. Sirijaraensre, B. Jansang, M. Ehara and J. Limtrakul, *RSC Adv.*, 2015, **5**, 97918–97927.
67 V. Parey, B. M. Abraham, S. H. Mir and J. K. Singh, *ACS Appl. Mater. Interfaces*, 2021, **13**, 35585–35594.
68 H. Song and D. E. Jiang, *Nanoscale*, 2023, **15**, 16010–16015.
69 S. Maier and M. Salmeron, *Acc. Chem. Res.*, 2015, **48**, 2783–2790.